THE ANISOTROPIC TRUNCATED KERNEL METHOD FOR CONVOLUTION WITH FREE-SPACE GREEN'S FUNCTIONS

LESLIE GREENGARD*, SHIDONG JIANG†, AND YONG ZHANG‡

Abstract. A common task in computational physics is the convolution of a translation invariant, free-space Green's function with a smooth and compactly supported source density. Fourier methods are natural in this context, but encounter two difficulties. First, the kernel is typically singular in Fourier space and second, the source distribution can be highly anisotropic. The truncated kernel method [49] overcomes the first difficulty by taking into account the spatial range over which the solution is desired and setting the Green's function to zero beyond that range in a radially symmetric fashion. The transform of this truncated kernel can be computed easily and is infinitely differentiable by the Paley-Wiener theorem. As a result, a simple trapezoidal rule can be used for quadrature, the convolution can be implemented using the FFT, and the result is spectrally accurate.

Here, we develop an anisotropic extension of the truncated kernel method, where the truncation region in physical space is a rectangular box, which may have a large aspect ratio. In this case, the Fourier transform of the truncated kernel is again smooth, but is typically not available analytically. Instead, an efficient sum-of-Gaussians approximation is used to obtain the Fourier transform of the truncated kernel efficiently and accurately. This then permits the fast evaluation of the desired convolution with a source distribution sampled on an anisotropic, tensor-product grid. For problems in d dimensions, the storage cost is $O(2^d N)$ independent of the aspect ratio, and the computational cost is $O(2^d N \log(2^d N))$, where N is the total number of grid points needed to resolve the density. The performance of the algorithm is illustrated with several examples.

Key words. Truncated kernel method, sum-of-Gaussian approximation, anisotropic density, FFT, Green's function

AMS subject classifications. 68Q25, 68R10, 68U05

1. Introduction.

In this paper, we consider the evaluation of convolution integrals of the form

$$\phi(\mathbf{x}) = [U * \rho](\mathbf{x}) = \int_{\mathbb{R}^d} U(\mathbf{x}-\mathbf{y})\rho(\mathbf{y})d\mathbf{y}, \tag{1.1}$$

where d is the ambient dimension, $\rho(\mathbf{x})$ is a smooth and compactly supported (or rapidly decaying) source distribution, and the convolution kernel $U(\mathbf{x})$ is a known radially symmetric function, which might be singular at the origin and/or at infinity. A typical example is the solution of the Poisson equation

$$-\Delta\phi = \rho$$

in free space, in which case $U(\mathbf{x}) = -\frac{1}{2\pi}\ln|\mathbf{x}|$ for $d = 2$ and $U(\mathbf{x}) = \frac{1}{4\pi|\mathbf{x}|}$ for $d = 3$.

It is well known from the convolution theorem that $\phi(\mathbf{x})$ in (1.1) can be computed

*Courant Institute of Mathematical Sciences, New York University, NY, United States and Flatiron Institute, Simons Foundation, New York, NY, United States, (greengard@cims.nyu.edu).

†Department of Mathematical Sciences, New Jersey Institute of Technology, Newark, New Jersey, 07102, USA (shidong.jiang@njit.edu). S. Jiang was supported by the National Science Foundation under grant DMS-1720405 and by the Flatiron Institute, a division of the Simons Foundation.

‡ Center for Applied Mathematics,Tianjin University,Tianjin 300072,China; Wolfgang Pauli Institute c/o Fak. Mathematik, University Wien, Oskar-Morgenstern-Platz 1, 1090 Vienna, Austria, (sunny5zhang@gmail.com). Y. Zhang was supported by Schrödinger Fellowship J3784-N32, the Austrian Science Foundation (FWF) under grant No. F41 (SFB "VICOM"), grant No. F65 (SFB "Complexity in PDEs") and the Wiener Wissenschafts und TechnologieFonds (WWTF) project No. MA16-066 ("SEQUEX").

in Fourier space by the formula

$$\phi(\mathbf{x}) = \frac{1}{(2\pi)^d} \int_{\mathbb{R}^d} \widehat{U}(\mathbf{k}) \widehat{\rho}(k) e^{i\mathbf{k}\cdot\mathbf{x}} d\mathbf{k}, \tag{1.2}$$

where the Fourier transform of f is defined as $\widehat{f}(\mathbf{k}) = \int_{\mathbb{R}^d} f(\mathbf{x}) e^{-i\mathbf{k}\cdot\mathbf{x}} d\mathbf{x}$. For the Coulomb potential (the Poisson equation), we have

$$\widehat{U}(\mathbf{k}) = \frac{1}{|\mathbf{k}|^2}. \tag{1.3}$$

This is, of course, true more generally; for any of the constant-coefficient partial differential equations of mathematical physics, the solution due to a source distribution $\rho(\mathbf{x})$ takes the form (1.1), (1.2), where $U(\mathbf{x})$ is the corresponding free-space Green's function. Important cases aside from the Coulomb potential include the Yukawa potential, the biharmonic potential, etc.

There is a substantial literature on alternative methods for the solution of partial differential equations in free space. Finite difference and finite element discretization of the governing equation, for example, are more flexible in terms of spatial adaptivity, but require the solution of large linear systems and the imposition of artificial, "outgoing" boundary conditions on the boundary of a finite computational domain. Integral transform methods, which compute (1.1) directly, avoid the need to *solve* a linear system or to impose artificial boundary conditions, but require quadrature schemes to handle the singularity of the kernel $U(\mathbf{x})$ and fast algorithms (such as the fast Fourier transform or the fast multipole method) to reduce the $O(N^2)$ cost, where N is the number of source and target points of interest (see, for example, [1, 2, 7, 14, 16, 23, 30, 33, 34, 37]).

Here, we are interested in the development of purely Fourier-based methods, sacrificing spatial adaptivity, but exploiting the speed of the FFT. The principal novelty of the present work is that we develop an effective method for the case where the source term ρ is strongly anisotropic, a situation which is frequently encountered in confined quantum systems [3, 4]. More precisely, we seek to develop an efficient method for (1.2) when ρ is given on a rectangular domain in d dimensions of the form

$$\mathbf{R}_{L\boldsymbol{\gamma}} = \prod_{j=1}^{d} [-L\gamma_j, L\gamma_j]\,. \tag{1.4}$$

We define the *anisotropy vector* by $\boldsymbol{\gamma} = (\gamma_1, \ldots, \gamma_d)$. The magnitudes of the γ_j reflect the degree of anisotropy. Without loss of generality, we assume that $\gamma_1 = 1$ and that $\gamma_j \leq 1$ for $j = 2, \ldots, d$. We also assume, for the sake of simplicity, that ρ is sampled on a grid with the same number of points in each linear dimension (achieving greater spatial resolution in the dimensions where γ_j is small).

Definition 1.1. *We will refer to*

$$\gamma_f := \prod_{j=2}^{d} \gamma_j^{-1} \tag{1.5}$$

as the anisotropy factor. *In the isotropic case, $\gamma_f = 1$, while for highly anisotropic source distributions, $\gamma_f \gg 1$.*

Leaving anisotropy aside for the moment, suppose that we approximate the integral in (1.2) by the trapezoidal rule (leading to a discrete Fourier transform). This, unfortunately, yields low order accuracy for the Poisson equation, because of the singularity in the kernel (1.3) (see [5, 6, 18]). While Jiang *et al.* developed a high order correction method in three dimensions that uses a spherical coordinate system near the origin [27], it requires the use of the nonuniform FFT (NUFFT) [15, 24]. This approach has been extended successfully to a variety of other kernels [6, 36], including the 2D Poisson kernel, where the $1/|\mathbf{k}|^2$ singularity cannot be obviated by simply changing to polar coordinates. Nevertheless, the needed modifications can become rather complicated when dealing with more general kernels, such as the Helmholtz kernel, where singularities are not restricted to the origin. Moreover, significant work would be required to extend these methods to the case of anisotropic grids.

A simpler and more efficient method is described in the recent paper by Vico *et al.* [49], which we refer to as the truncated kernel method (TKM). It is based on the observation that, if one seeks the solution to the convolution equation (1.2) only in a ball B of radius R, with the source distribution supported in B as well, then no error is incurred by convolving with $U_B(\mathbf{x})$ instead of $U(\mathbf{x})$, where

$$U_B(\mathbf{x}) = \begin{cases} U(\mathbf{x}) & \text{for } |\mathbf{x}| \leq 2R \\ 0 & \text{for } |\mathbf{x}| > 2R. \end{cases}$$

This is clear from inspection of the formula (1.1); the maximum distance of a target point of interest from a source point is $2R$. The truncated kernel $U_B(\mathbf{x})$ is compactly supported, so that $\widehat{U}_B(\mathbf{k})$ is entire (and C^∞) by the Paley-Wiener Theorem (see, for example, [44]). It is, in fact, straightforward to show that

$$\widehat{U}_B(\mathbf{k}) = \frac{1 - \cos(2|\mathbf{k}|R)}{|\mathbf{k}|^2}. \tag{1.6}$$

In short, the TKM replaces (1.2) with

$$\phi(\mathbf{x}) = \frac{1}{(2\pi)^d} \int_{\mathbb{R}^d} \widehat{U}_B(\mathbf{k}) \widehat{\rho}(\mathbf{k}) e^{i\mathbf{k}\cdot\mathbf{x}} d\mathbf{k}. \tag{1.7}$$

Note that for the source distribution in (1.4), we have

$$R = L\sqrt{1 + \gamma_1^2 + \cdots + \gamma_d^2}. \tag{1.8}$$

Although smooth, $\widehat{U}_B$ decays slowly in the Fourier domain. It is the smoothness of the source distribution that provides the needed high-frequency cut-off in (1.2). Combining these observations, it follows that trapezoidal rule discretization of (1.7) and the FFT lead to a spectrally accurate method. This idea was introduced in the Coulomb setting as the "supercell" method [26, 43], and in the Helmholtz setting by Vainikko [48]. The TKM [49] developed this approach in some generality and derived analytic formulas for $\widehat{U}_B(\mathbf{k})$ in connection with many physically important problems including the Coulomb, Helmholtz, biharmonic, and constant-coefficient advection-diffusion kernels in both two and three dimensions. It has recently been extended to systems with periodicity in a subset of directions in [45].

Returning now to the issue of anisotropy, let us assume that the source ρ is resolved in physical space with a grid whose grid spacing in the jth coordinate direction is $\Delta x_j = L\gamma_j/n$. By standard results in Fourier analysis [47], it follows that

$$\Delta k_j = \frac{\pi}{L\gamma_j} \tag{1.9}$$

is sufficient to resolve $\widehat{\rho}(\mathbf{k})$. Using the TKM, however, we would first need to enclose the rectangular box $\mathbf{R}_{L\boldsymbol{\gamma}}$ from (1.4) in a sphere. As noted above, however, the radius of the smallest such sphere is given by (1.8) in d dimensions and the isotropically truncated kernel $\widehat{U}_B$ requires that

$$\Delta k_j < \frac{\pi}{2R} \tag{1.10}$$

in each coordinate direction. This can be seen either from inspection of the $\cos(2|\mathbf{k}|R)$ term in (1.6) and the Nyquist-Shannon sampling theorem or from consideration of "local-global duality" in the Fourier transform [47]. As a result, to reach the desired resolution requires a factor of γ_f more points in Fourier space than needed to resolve the source distribution itself. A further oversampling factor of 2^d is needed in order to carry out aperiodic convolution (but that holds for any FFT-based scheme). In short, the excessively fine Δk_j needed to resolve $\widehat{U}_B(\mathbf{k})$ in (1.10) compared to that needed to resolve $\widehat{\rho}(\mathbf{k})$ in (1.9) makes the TKM prohibitively expensive for highly anisotropic problems.

In this paper, we propose an anisotropic truncated kernel method (ATKM) to handle anisotropic problems while avoiding the extra cost induced by the anisotropy factor γ_f. Instead of truncating the convolution kernel in a radially symmetric fashion, we set the kernel to zero outside a rectangular box that is twice the size of $\mathbf{R}_{L\boldsymbol{\gamma}}$ in each direction. That is, we let $U_R(\mathbf{x}) = U(\mathbf{x})\chi_{\mathbf{R}_{2L\boldsymbol{\gamma}}}(\mathbf{x})$. Since the truncated kernel $U_R(\mathbf{x})$ now has the same anisotropic structure as the source ρ, this eliminates the need for uniform sampling in Fourier space when computing the inverse Fourier transform in (1.7). On the other hand, the truncated kernel in the Fourier domain now takes the form

$$\widehat{U}_R(\mathbf{k}) = \int_{\mathbb{R}^d} U_R(\mathbf{x}) e^{-i\mathbf{k}\cdot\mathbf{x}} d\mathbf{x} = \int_{\mathbf{R}_{2L\boldsymbol{\gamma}}} U(\mathbf{x}) e^{-i\mathbf{k}\cdot\mathbf{x}} d\mathbf{x}, \quad \mathbf{k} \in \mathbb{R}^d. \tag{1.11}$$

It no longer has an explicit analytical expression, even if the original kernel is radially symmetric. Instead, it must be computed numerically. For this, we approximate the kernel $U(\mathbf{x})$ by a sum of Gaussians $U_{GS}(\mathbf{x})$ for $|\mathbf{x}| \in [\delta, 2R]$, where δ is a cut-off parameter to be determined and R is given by (1.8).

That is, for a prescribed precision ε, we assume that

$$\|U(\mathbf{x}) - U_{GS}(\mathbf{x})\| < \varepsilon \|U(\mathbf{x})\|, \qquad \delta \le |\mathbf{x}| \le 2R, \tag{1.12}$$

where

$$U_{GS}(\mathbf{x}) = \sum_{i=1}^{S} w_i e^{-s_i|\mathbf{x}|^2}. \tag{1.13}$$

We may then write

$$\widehat{U}_R(\mathbf{k}) = \int_{\mathbf{R}_{2L\boldsymbol{\gamma}}} U_{GS}(\mathbf{x}) e^{-i\mathbf{k}\cdot\mathbf{x}} d\mathbf{x} + \int_{\mathbf{B}_\delta} [U(\mathbf{x}) - U_{GS}(\mathbf{x})] e^{-i\mathbf{k}\cdot\mathbf{x}} d\mathbf{x} + O(\varepsilon), \tag{1.14}$$

where $\mathbf{B}_\delta$ is the ball of radius δ.

It remains to find an efficient sum of Gaussians approximation for the first integral in (1.14) and a suitable asymptotic method to compute the second integral. We can then provide a complete description of the algorithm.

REMARK 1. *The approximation of the convolution kernel in physical space by a sum of Gaussians has been studied extensively in [10, 11, 9, 12, 17, 20, 21, 25, 35]. The paper [17], in particular, is closely related to the present work. There, the convolution is split into a singular near-field component, computed using a Taylor expansion of the density and a regular far-field component, computed using a sum-of-Gaussians approximation of the kernel. Both can be evaluated via the FFT.*

REMARK 2. *The reason a sum-of-Gussians approximation is particularly useful is that it permits the first (d-dimensional) integral in (1.14) to be computed as a product of d one-dimensional integrals - that is, it permits* separation of variables. *Thus, the cost of evaluating these one-dimensional integrals is only $O(SN^{1/d})$, where N is the total number of discretization points in either physical or Fourier space.*

The cutoff parameter δ is chosen sufficiently small that a low-order asymptotic expansion yields sufficient accuracy and requires only $O(S+N)$ work for the evaluation of the second integral in (1.14).

REMARK 3. *There have been other FFT based fast algorithms developed for the calculation of convolution-type integrals. These include the pre-corrected FFT for computing convolution integrals when the discretization points are close to but not exactly on a regular grid (see, for example, [40, 41, 50]) and Particle Mesh Ewald method for systems involving periodic conditions in certain directions (see, for example, [13, 31, 32, 46]). We do not intend to present a comprehensive review of these algorithms here, and refer the reader to the aforementioned references for details.*

The paper is organized as follows. We show, in section 2, that the number of Gaussians S is of the order $S = O(\log\delta \log\varepsilon)$ for a variety of non-oscillatory kernels with radial symmetry. In section 3, we present the ATKM with detailed error analysis and parameter selection strategies. In section 4, we illustrate the performance of the algorithm with several numerical examples. Some concluding remarks can be found in section 5.

2. Sum-of-Gaussian approximation of convolution kernels. In this section, we first consider the three-dimensional Yukawa (or modified Helmholtz) kernel $\frac{e^{-\lambda r}}{4\pi r}$, i.e., the Green's function for the partial differential equation $(-\Delta+\lambda^2)u = \rho$. The 3D Coulomb kernel (corresponding to $\lambda = 0$) and the general power function $\frac{1}{r^\beta}$ with $\beta > 0$, have been studied in detail in [11].

We begin with the integral representation

$$\frac{e^{-\lambda r}}{4\pi r} = \frac{1}{2\pi\sqrt{\pi}}\int_0^\infty e^{-r^2t^2-\frac{\lambda^2}{4t^2}}dt = \frac{1}{2\pi\sqrt{\pi}}\int_{\mathbb{R}} e^{-r^2e^{2u}}e^{-\frac{\lambda^2}{4}e^{-2u}}e^u\,du, \tag{2.1}$$

where the first equality can be found in [8], and the second equality follows from change of variable $t = e^u$. The representation can be viewed as an integral of a Gaussian kernel with respect to the r variable so that a discrete sum-of-Gaussians approximation can be obtained by discretization.

LEMMA 2.1. *Let $[\delta, L]$ denote an interval with $0 < \delta < R$. Then*

$$\|\frac{e^{-\lambda r}}{4\pi r} - U_{GS}(r)\| = O(e^{-C_1 M/\log M}) \tag{2.2}$$

where

$$U_{GS}(r) = \sum_{j=-M}^{M}\omega_j e^{-\tau_j^2 r^2}, \tag{2.3}$$

with $\omega_j = \frac{1}{4\pi}\frac{2}{\sqrt{\pi}} h\, e^{u_j} e^{-\frac{\lambda^2}{4} e^{-2u_j}}$, $u_j = j\,h, \tau_j = e^{u_j}$, *and* $h = \log\left(\frac{2\pi a M}{b}\right)/(aM)$.

Proof. As a function of u, the integrand $f(u) := e^{-r^2 e^{2u}} e^{-\frac{\lambda^2}{4} e^{-2u}} e^u$ lies in $H^1(D_l)$ for $l < \pi/2$ [25], containing all holomorphic functions in the strip $D_l := \{\mathbf{z} \in \mathbb{C} : |\operatorname{Im} z| \le l\}$, satisfying the additional property

$$N(f, D_l) := \int_{\partial D_l} |f(\mathbf{z})|\,|d\mathbf{z}| = \int_{\mathbb{R}} \left(|f(u+il)| + |f(u-il)|\right) \mathrm{d}\,u < \infty. \tag{2.4}$$

We also have that $|f(u)| \le Ce^{-be^{a|u|}}$ with $a = 2$, $b = \min\{\delta^2, \lambda^2/4\}$ for all $u \in \mathbb{R}$ and $r \in [\delta, R]$. Thus, by Proposition 2.1 in [25], the truncated trapezoidal rule applied to (2.1) leads to a spectrally accurate approximation. ∎

REMARK 4. *In practice, we change the summation limits in* (2.3) *to* M_1 *and* M_2 *by finding a range for* u *in* (2.1) *beyond which the integrand is negligible. We then apply standard model reduction algorithm (see, for example, [51]) to reduce the number of Gaussians as a final optimization step.*

Table 2.1 shows the number of terms for various values of δ and ε over the interval $[\delta, 16\sqrt{3}]$ for $\lambda = 1$, where the desired accuracy ε is measured in the relative maximum norm. Note that the number of terms grows linearly (or sublinearly) in terms of both $\log(\varepsilon^{-1})$ and $\log(\delta^{-1})$.

TABLE 2.1
Number of Gaussians needed for approximating the 3D Yukawa kernel $U(r) = \frac{1}{4\pi}\frac{e^{-\lambda r}}{r}$ *over* $[\delta, 16\sqrt{3}]$ *with* $\lambda = 1$ *for the given accuracy* ε.

$\delta \setminus \varepsilon$	10^{-6}	10^{-7}	10^{-8}	10^{-9}	10^{-10}	10^{-11}	10^{-12}
10^{-3}	33	38	44	49	55	60	67
10^{-4}	40	46	53	60	67	73	80
10^{-5}	47	54	62	70	78	85	93
10^{-6}	54	62	72	80	90	98	107

For the 2D Yukawa kernel $\frac{1}{2\pi}K_0(\lambda r)$, where K_0 is the modified Bessel function of the second kind of order 0 (Section 10.25 in [39]), we may start from the integral representation (eq. 10.32.10 in [39])

$$U_\lambda(r) = \frac{1}{2\pi}K_0(\lambda r) = \frac{1}{4\pi}\int_0^\infty e^{\left(-t - \frac{\lambda^2 r^2}{4t}\right)}\frac{dt}{t} = \frac{1}{4\pi}\int_{\mathbb{R}} e^{-\frac{\lambda^2 r^2}{4}e^{-u} - e^u}\,du. \tag{2.5}$$

We then follow a similar procedure to obtain an efficient, accurate sum-of-Gaussians approximation.

2.1. A black-box algorithm for the Gaussian-sum approximation of radially symmetric kernels. Assume now that the kernel is radially symmetric, i.e., $U(\mathbf{x}) = U(r)$, $r = |\mathbf{x}|$. Then the problem is reduced to one-dimensional approximation problem. By a simple change of variable $r = \sqrt{x}$, we observe that the sum-of-Gaussian approximation of $U(r)$ on $[\delta, R]$ is equivalent to the sum-of-exponential approximation of $U(\sqrt{x})$ on $[\delta^2, R^2]$. Sum-of-exponential approximations have been studied more extensively in literature (see, for example, [10, 11]). However, [10] samples the function using equispaced points; while [11] considers the power functions only. Here we consider sum-of-exponential approximation of a nonoscillatory function $f(x)$ on an interval $[a, b] \subset \mathbb{R}^+$. We assume that f is in general singular at the origin, as is

the case for most Green's functions, and the left end point a may be very close to the origin. Thus, the method in [10] does not seem to be a very effective method for finding sum-of-exponential approximation of f.

As is well known, the Laplace transform of an exponential function $e^{-\alpha t}$ is the pole function $\frac{1}{s+\alpha}$. In [51], a bootstrap method for finding sum-of-pole approximations for a certain class of function is developed. The method applies a nonlinear least squares procedure recursively on a successively larger interval on the imaginary axis. The method in [51] tries to find the sum-of-pole approximation for a given function such that the approximation is valid in the entire right half of the complex plane; while our objective here is to find a Gaussian-sum approximation on a finite interval.

We have developed a simplified algorithm for finding the sum-of-exponential approximation. The algorithm consists of two stages (see [28] for details). In the first stage, a preliminary sum-of-exponential approximation that is accurate but inefficient is constructed for f on $[a, b]$. That is,

$$f(x) \approx \sum_{j=1}^{P} \tilde{w}_j e^{\tilde{s}_j x}, \qquad x \in [a, b]. \tag{2.6}$$

This is done as follows. We first allocate a set of P logarithmically equally spaced points $\tilde{s}_j$ $(j = 1, \ldots, P)$ lying on the negative real axis, which serve as the nodes in the preliminary sum-of-exponential approximation (2.6). Second, a set of sampling points on $[a, b]$ are constructed via adaptive bisections into smaller and smaller subintervals such that the given function f is accurately approximated by a Chebyshev polynomial of degree no greater than n_c on each subinterval. Since the origin is assumed to be a singular point, we further make dyadic subdivisions for the interval close to the origin. We denote these sampling points by x_i, $i = 1, \ldots, M$. We now solve the following linear least squares problem

$$A\tilde{w} = b, \tag{2.7}$$

where A is an $M \times P$ matrix with the entry $A_{ij} = e^{\tilde{s}_j x_i}$, $\tilde{w}$ is a column vector of length P containing the weights in the preliminary sum-of-exponential approximation, and b is a column vector of length M with $b_i = f(x_i)$.

In the second stage, we apply the "squareroot method" in model reduction (see, for example, [51] and references therein for details) to reduce the number of exponentials to achieve a near optimal sum-of-exponential approximation. That is,

$$\sum_{j=1}^{P} \tilde{w}_j e^{\tilde{s}_j x} \approx \sum_{j=1}^{S} w_j e^{s_j x}. \tag{2.8}$$

The optimality of the resulting sum-of-exponential approximation in L^∞ norm is guaranteed by well-known results in control theory (see, for example, [22]). We would like to remark that the model reduction technique was originally designed for sum-of-pole approximations. However, since all the nodes lie in the left half of the complex plane, we may apply it directly to the reduction of sum-of-exponential approximation due to the aforementioned connection between these two types of approximations.

Taking now $f(x) = U(\sqrt{x})$, $[a, b] = [\delta^2, R^2]$, and combining (2.6) and (2.8), we obtain

$$U(\mathbf{x}) = U(r) = U(x) \approx \sum_{j=1}^{S} w_j e^{s_j x^2}, \qquad x \in [\delta, R]. \tag{2.9}$$

We have applied the algorithm to find efficient and accurate Gaussian-sum approximations for many kernels, including the biharmonic Green's function in both two and three dimensions, the Poisson kernel in two dimensions, etc. The performance of the algorithm on these kernels is similar. Table 2.2 lists the number of Gaussians needed to approximate the 2D Poisson kernel $-\frac{1}{2\pi}\ln|\mathbf{x}|$ on the interval $[\delta, R]$ with various δ and relative L^2 error bound ε.

TABLE 2.2
Number of Gaussians needed for approximating the 2D Poisson kernel $U(r) = -\frac{1}{2\pi}\ln(r)$ over $[\delta, 2\sqrt{2}]$ for the given accuracy ε.

$\delta \setminus \varepsilon$	10^{-6}	10^{-7}	10^{-8}	10^{-9}	10^{-10}	10^{-11}	10^{-12}
10^{-3}	80	86	95	107	117	128	137
10^{-4}	98	109	124	136	152	160	171
10^{-5}	118	134	146	164	189	196	209
10^{-6}	131	151	167	195	214	231	241

3. Anisotropic truncated kernel method. We now discuss the ATKM in detail. We assume that the density function ρ is compactly supported in a generally anisotropic rectangular box $\mathbf{R}_{L\boldsymbol{\gamma}}$ and well resolved by n equispaced points in each direction. Thus, the total number of grid points needed to resolve the density function ρ on $\mathbf{R}_{L\boldsymbol{\gamma}}$ is $N = n^d$. We truncate the kernel on a rectangular box $\mathbf{R}_{2L\boldsymbol{\gamma}}$ instead of an isotropic ball. That is,

$$\begin{aligned}\phi(\mathbf{x}) &= \int_{\mathbb{R}^d} U(\mathbf{y})\rho(\mathbf{x}-\mathbf{y})d\mathbf{y} = \int_{\mathbf{x}+\mathbf{R}_{L\boldsymbol{\gamma}}} U(\mathbf{y})\rho(\mathbf{x}-\mathbf{y})d\mathbf{y} \\ &= \int_{\mathbf{R}_{2L\boldsymbol{\gamma}}} U(\mathbf{y})\rho(\mathbf{x}-\mathbf{y})d\mathbf{y}, \qquad \mathbf{x}\in\mathbf{R}_{L\boldsymbol{\gamma}}.\end{aligned} \tag{3.1}$$

For the density $\rho(\mathbf{x}-\mathbf{y})$ in (3.1), we have $\mathbf{x}-\mathbf{y}\in\mathbf{R}_{3L\boldsymbol{\gamma}}$ for $\forall\,\mathbf{x}\in\mathbf{R}_{L\boldsymbol{\gamma}}, \mathbf{y}\in\mathbf{R}_{2L\boldsymbol{\gamma}}$. Therefore we can approximate the density ρ on $\mathbf{R}_{3L\boldsymbol{\gamma}}$ by a Fourier pseudo-spectral method with spectral accuracy [47]. This seems to require a threefold zero-padding from $\mathbf{R}_{L\boldsymbol{\gamma}}$ to $\mathbf{R}_{3L\boldsymbol{\gamma}}$. However, straightforward analysis shows that to obtain the solution in the domain $\mathbf{R}_{L\boldsymbol{\gamma}}$ itself, it is sufficient to carry out zero-padding to $\mathbf{R}_{2L\boldsymbol{\gamma}}$. In short, the density ρ is well resolved by the following finite Fourier series

$$\rho(\mathbf{z}) \approx \sum_{\mathbf{k}} \widehat{\rho}_{\mathbf{k}}\, e^{i\mathbf{k}\cdot\mathbf{z}}, \qquad \mathbf{z}\in\mathbf{R}_{2L\boldsymbol{\gamma}}, \tag{3.2}$$

where $\mathbf{k} = \frac{\pi}{2L}(\frac{k_1}{\gamma_1},\ldots,\frac{k_d}{\gamma_d})$ with $k_j = -n,\ldots,n-1$ for $j = 1,\ldots,d$. The Fourier coefficients are given by the formula

$$\widehat{\rho}_{\mathbf{k}} = \frac{1}{|\mathbf{R}_{2L\boldsymbol{\gamma}}|}\int_{\mathbf{R}_{2L\boldsymbol{\gamma}}} \rho(\mathbf{z})e^{-i\mathbf{k}\cdot\mathbf{z}}d\mathbf{z}, \tag{3.3}$$

where $|\mathbf{R}_{2L\boldsymbol{\gamma}}| = (4L)^d\prod_{j=1}^d\gamma_j$ is the volume of $\mathbf{R}_{2L\boldsymbol{\gamma}}$.

By the assumption on ρ, the integral in (3.3) is well approximated by the trapezoidal rule. Thus $\widehat{\rho}_{\mathbf{k}}$ can be evaluated via the forward FFT of size 2^dN. Using (3.1) and (3.2), we obtain

$$\begin{aligned}\phi(\mathbf{x}) &= \int_{\mathbf{R}_{2L\boldsymbol{\gamma}}} U(\mathbf{y})\rho(\mathbf{x}-\mathbf{y})d\mathbf{y} \\ &\approx \sum_{\mathbf{k}} \widehat{\rho}_{\mathbf{k}} e^{i\mathbf{k}\cdot\mathbf{x}} \left(\int_{\mathbf{R}_{2L\boldsymbol{\gamma}}} U(\mathbf{y}) e^{-i\mathbf{k}\cdot\mathbf{y}} d\mathbf{y} \right) \\ &:= \sum_{\mathbf{k}} \widehat{U}_R(\mathbf{k})\ \widehat{\rho}_{\mathbf{k}}\ e^{i\mathbf{k}\cdot\mathbf{x}},\end{aligned} \tag{3.4}$$

where $\widehat{U}_R(\mathbf{k})$ is defined by the formula

$$\boxed{\widehat{U}_R(\mathbf{k}) := \int_{\mathbf{R}_{2L\boldsymbol{\gamma}}} U(\mathbf{y}) e^{-i\mathbf{k}\cdot\mathbf{y}} d\mathbf{y}.} \tag{3.5}$$

Clearly, once $\widehat{U}_R(\mathbf{k})$ is available, the evaluation of the potential ϕ can be accomplished in three simple steps: (1) a forward FFT of size $2^d N$ for computing $\widehat{\rho}(\mathbf{k})$, (2) pointwise multiplication of $\widehat{U}_R(\mathbf{k})$ and $\widehat{\rho}(\mathbf{k})$, and (3) a backward FFT of size $2^d N$ for computing $\phi(\mathbf{x})$. An alternative derivation of the procedure can be obtained from the Fourier integral representation (1.2) rather than the convolution form to derive (3.4). We prefer the derivation above because it is easier to verify that twofold zero-padding along each direction is necessary and sufficient for the evaluation of the potential.

In order to compute $\widehat{U}_R(\mathbf{k})$, we apply the Gaussian-sum approximation of the kernel to split the integral into two parts as in (1.14). That is,

$$\widehat{U}_R(\mathbf{k}) \approx I_1(\mathbf{k}) + I_2(\mathbf{k}), \tag{3.6}$$

where

$$I_2(\mathbf{k}) = \int_{B_\delta} (U - U_{\mathrm{GS}})(\mathbf{y}) e^{-i\mathbf{k}\cdot\mathbf{y}} d\mathbf{y} \tag{3.7}$$

and

$$\begin{aligned} I_1(\mathbf{k}) &= \int_{\mathbf{R}_{2L\boldsymbol{\gamma}}} U_{GS}(\mathbf{y}) e^{-i\mathbf{k}\cdot\mathbf{y}} d\mathbf{y} = \int_{\mathbf{R}_{2L\boldsymbol{\gamma}}} \sum_{i=1}^{S} w_i\, e^{s_i|\mathbf{y}|^2} e^{-i\mathbf{k}\cdot\mathbf{y}} d\mathbf{y} \\ &= \sum_{i=1}^{S} w_i \prod_{j=1}^{d} G_{ij}(s_i, k_j), \end{aligned} \tag{3.8}$$

with

$$G_{ij}(s_i, k_j) = \int_{-2L\gamma_j}^{2L\gamma_j} e^{s_i y_j^2} e^{\frac{-\pi i\ k_j\ y_j}{2L\gamma_j}} dy_j, \quad i = 1, \ldots, S, \quad k_j = -n, \ldots, n-1. \tag{3.9}$$

The last equality in (3.8) follows from the separable structure of Gaussians. We observe that the d-dimensional integral is decomposed into d one-dimensional Fourier integrals of the Gaussians, leading to great reduction in the computational cost. Let $\alpha^2 = -s_i L^2 \gamma_j^2$, $\beta = \pi k_j/2$, and $x = y_j/(L\gamma_j)$. These one-dimensional integrals are

reduced to the following standard form

$$\begin{aligned}\frac{G_{ij}(s_i,k_j)}{L\gamma_j} &= G(\alpha,\beta) = \int_{-2}^{2} e^{-\alpha^2x^2} e^{-i\frac{\pi k x}{2}} dx \\ &= \frac{\sqrt{\pi}}{\alpha} e^{-\frac{\beta^2}{4\alpha^2}} \left[\mathrm{erf}\left(-2\alpha + i\frac{\beta}{2\alpha})\right) - \mathrm{erf}\left(2\alpha + i\frac{\beta}{2\alpha})\right)\right] \\ &= \frac{\sqrt{\pi}}{\alpha} e^{-\frac{\beta^2}{4\alpha^2}} - \frac{\sqrt{\pi}}{\alpha} e^{-4\alpha^2} \mathrm{Re}\left(e^{-i\pi k_j}\omega\left(-\frac{\beta}{2\alpha} + 2i\alpha\right)\right).\end{aligned} \tag{3.10}$$

Here $\mathrm{erf}(z) = \frac{2}{\sqrt{\pi}}\int_0^z e^{-t^2}dt$ is the error function [39] and $\omega(z) = e^{-z^2}(1-\mathrm{erf}(-iz))$ is the so-called Faddeeva function [19, 42, 52], which can be evaluated easily via existing software package [29]. After the evaluation of these $2dSn = 2dSN^{1/d}$ one-dimensional integrals, $I_1(\mathbf{k})$ can be evaluated in $O(S2^dN)$ multiplications and additions. Thus the computation of $I_1(\mathbf{k})$ is very cheap, even though S may be in the order of 100. We remark here that it is embarrassingly easy to parallelize this step, leading to further reduction on the computational time if needed.

For $I_2(\mathbf{k})$, we expand the plane-wave function into Taylor series and calculate the integral term by term. That is,

$$I_2(\mathbf{k}) \approx \int_{B_\delta} (U - U_{\mathrm{GS}})(\mathbf{y}) T(\mathbf{y}) d\mathbf{y}, \tag{3.11}$$

where $T(\mathbf{y})$ is the truncated Taylor expansion of the complex exponential $e^{-i\mathbf{k}\cdot\mathbf{y}}$ of order p. Since $U - U_{\mathrm{GS}}$ is radially symmetric, any term involving $\mathbf{y}^\alpha := \prod_{j=1}^d y_j^{\alpha_j}$ with some odd α_j vanishes by symmetry. Hence, we only need to compute those even power terms. The lowest order term is simply the integral of $U - U_{\mathrm{GS}}$ itself. And the second order terms can be calculated as follows

$$\int_{B_\delta} (U - U_{\mathrm{GS}})(\mathbf{y}) y_j^2 d\mathbf{y} = \frac{2^{d-1}\pi}{d}\int_0^\delta (U - U_{\mathrm{GS}})(r) r^{d+1} dr. \tag{3.12}$$

This integral may be computed semianalytically for many kernels. For example, if U is the 3D Coulomb kernel, then

$$\int_{B_\delta} (U - U_{\mathrm{GS}})(\mathbf{y}) y_j^2 d\mathbf{y} = \frac{4\pi}{3}\int_0^\delta \left(\frac{1}{4\pi}\frac{1}{r} - \sum_{i=1}^S w_i e^{s_i r^2}\right) r^4 dr = \frac{\delta^4}{12} - \frac{4\pi}{3}\sum_{i=1}^S w_i F(s_i,\delta),$$

where $F(s_i,\delta) = \int_0^\delta e^{s_i r^2} r^4 dr$. As k_j can be pulled out when evaluating these integrals, the computational cost of evaluating $I_2(\mathbf{k})$ is $O(Sp+N)$ or simply $O(N)$ as $Sp \ll N$ in practice.

We now discuss the choice of the parameter δ. δ should be chosen so that the truncation error of the Taylor expansion is uniformly bounded for all $\mathbf{k}$ in the computational range. That is, if we write

$$E_T(\mathbf{k}) = \int_{B_\delta} (U - U_{\mathrm{GS}})(\mathbf{y})(e^{-i\mathbf{k}\cdot\mathbf{y}} - T(\mathbf{y}))d\mathbf{y}, \tag{3.13}$$

where $T(\mathbf{y})$ is the Taylor expansion of the complex exponential $e^{-i\mathbf{k}\cdot\mathbf{y}}$ to the p-th order, then we require that

$$|E_T(\mathbf{k})| \le \varepsilon \tag{3.14}$$

for all $\mathbf{k}$ in the computational range. For the 3D Coulomb kernel, we have

$$|E_T(\mathbf{k})| = C\left(\frac{\pi|k|\delta}{2L\gamma_j}\right)^{p+4}, \quad |k| = 1,\ldots,n,\ j = 1,\ldots,d. \tag{3.15}$$

Combining (3.14) and (3.15), we obtain

$$\delta \approx \frac{2L\varepsilon^{1/(p+4)}}{\pi N^{1/d}} \min_j \gamma_j. \tag{3.16}$$

For example, if $L = 8$, $p = 2$, $\varepsilon = 2 \times 10^{-16}$, $n = N^{1/d} = 128$, $\min_j \gamma_j = \frac{1}{16}$, then (3.16) leads to $\delta \approx 6 \times 10^{-6}$.

Algorithm 3.1 Anisotropic truncated kernel method

Comment: Given a precision requirement ε, the computational box $\mathbf{R}_{L\boldsymbol{\gamma}}$, the convolution kernel U, and the density ρ, compute the potential defined in (1.1).

1: Precomputation stage: determine δ and find the Gaussian-sum approximation of the kernel U on $[\delta, 2R]$.
2: Compute $2dSn$ one-dimensional integrals $G_{ij}(s_i, k_j)$ via (3.10).
3: Compute $I_1(\mathbf{k})$ via (3.8).
4: Compute $I_2(\mathbf{k})$ via (3.11).
5: Compute the Fourier transform of the truncated kernel $\widehat{U}_R(\mathbf{k})$ by adding $I_1(\mathbf{k})$ and $I_2(\mathbf{k})$.
6: Compute $\widehat{\rho}_{\mathbf{k}}$ via the forward FFT.
7: Compute the product $\widehat{U}_R(\mathbf{k})\widehat{\rho}(\mathbf{k})$.
8: Compute $\phi(\mathbf{x})$ via the backward FFT.

We summarize the algorithm in Algorithm 3.1. The second step requires $O(SN^{1/d})$ work; the third step requires $O(SN)$ work; the fourth step requires $O(S+N)$ work; the fifth and seventh steps require $O(N)$ work; and the sixth and eighth steps require $O(N \log N)$ work. As noted before, S depends on δ and ε logarithmically. Combining this observation with (3.16), we have $S = O(\log N \log \varepsilon)$. Hence, the total computational cost is $O(N \log N)$. Here we also note that the evaluation of $\widehat{U}_R(\mathbf{k})$ (i.e., steps 1–5 in the algorithm) need to be done only once for many time-dependent problems or problems with fixed geometry.

Finally, we would like to emphasize that the main advantage of the ATKM in this paper, as compared with the TKM in [49], is that one does not need excessive zero-padding for highly anisotropic problems. Figure 3.1 illustrates different zero-paddings of the TKM and the ATKM for an anisotropic density in two dimensions. The density $\rho(\mathbf{x})$ is assumed to be compactly supported in $\mathbf{R}_{L\boldsymbol{\gamma}} = [-1,1] \times [-\gamma,\gamma]$ (here $\gamma = \frac{1}{4}$). The TKM in [49] requires that the physical domain be enlarged to $[-2,2] \times [-2,2]$ via zero-padding, i.e., a factor of $2^2/\gamma = 16$ increase in the number of discretization points. For the ATKM, the physical domain needs only to be enlarged to $[-2,2] \times [-\frac{1}{2},\frac{1}{2}]$, i.e., a factor of $2^2 = 4$ increase. The savings in the ATKM become even greater for three dimensional highly anisotropic problems. It should also be noted that the TKM requires an initialization phase with oversampling by a factor of 4 in each linear dimension rather than two [49]. This would increase the memory requirements, but can be obviated by decomposing the precomputation into smaller subproblems.

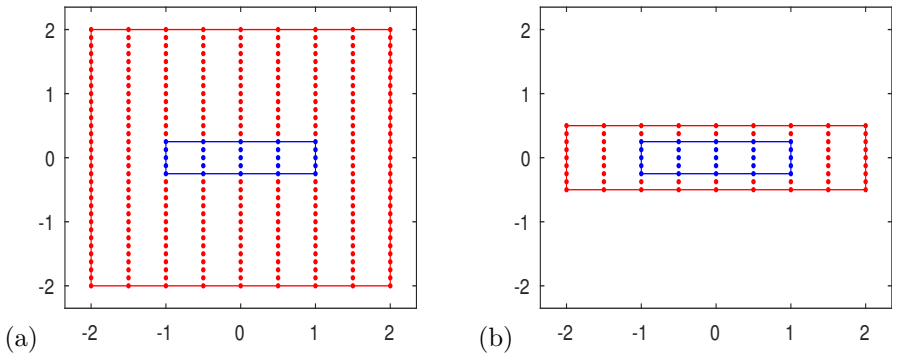

FIG. 3.1. *Meshing strategies of the TKM (a) and the ATKM (b) for an anisotropic density $\rho(\boldsymbol{x})$ that is compactly supported in $[-1,1]\times[-\frac{1}{4},\frac{1}{4}]$ (labeled in blue). The zero-padded grid points are plotted in red. The zero-padded physical domain is $[-2,2]\times[-2,2]$ and $[-2,2]\times[-\frac{1}{2},\frac{1}{2}]$ for the TKM and the ATKM, respectively.*

3.1. Error estimates. To derive error estimates of the algorithm, we only have to analyze the error of computing (3.5) via (3.6)–(3.11), as all other approximations are of spectral accuracy. Straightforward inspection shows that the error consists of two parts - the error due to the Gaussian-sum approximation of the kernel on $\mathbf{R}_{2L\boldsymbol{\gamma}}\backslash B_\delta$ and the error due to the truncated Taylor expansion of the complex exponential. That is

$$E(\mathbf{k}) = E_{GS}(\mathbf{k}) + E_T(\mathbf{k}), \tag{3.17}$$

where $E_{GS}(\mathbf{k}) = \int_{\mathbf{R}_{2L\boldsymbol{\gamma}}\backslash B_\delta}(U-U_{\rm GS})(\mathbf{y})e^{-i\mathbf{k}\cdot\mathbf{y}}d\mathbf{y}$ and $E_T(\mathbf{k})$ is given by (3.13). Using the Cauchy-Schwarz inequality, we have

$$\begin{aligned}|E_{GS}(\mathbf{k})| &\le \int_{\mathbf{R}_{2L\boldsymbol{\gamma}}\backslash B_\delta}|U-U_{\rm GS}|d\mathbf{y} \le S^{d-1}\int_\delta^{2R}|U-U_{\rm GS}|(r)\ r^{d-1}\,dr\\ &\le \varepsilon\ \frac{S^{d-1}}{(2d-1)^{1/2}}\ \|U\|_{L^2([\delta,2R])}\ (2R)^{d-1/2},\end{aligned} \tag{3.18}$$

with $R = L\sqrt{\sum_j \gamma_j^2}$ and $S^{d-1} = \frac{2\pi^{\frac{d}{2}}}{\Gamma(d/2)}$. For $E_T(\mathbf{k})$, the choice of δ in (3.16) guarantees that $|E_T(\mathbf{k})| \le \varepsilon$ for all $\mathbf{k}$ in the computational range. Therefore, the error can be controlled to any prescribed precision.

4. Numerical Results. To demonstrate the accuracy and efficiency of the ATKM, we carry out several numerical experiments. All numerical errors are calculated in the relative maximum norm, defined as follows:

$$E := \frac{\|\phi-\phi_{\vec{h}}\|_{l^\infty}}{\|\phi\|_{l^\infty}} = \frac{\max_{\mathbf{x}\in\mathcal{T}_h}|\phi(\mathbf{x})-\phi_{\vec{h}}(\mathbf{x})|}{\max_{\mathbf{x}\in\mathcal{T}_h}|\phi(\mathbf{x})|}, \tag{4.1}$$

where $\mathcal{T}_h$ is the rectangular computational domain discretized uniformly in each direction with mesh size vector $\vec{h} = (h_1,\ldots,h_d)^T$. Here, the grid function $\phi_{\vec{h}}$ is the numerical solution and ϕ is the exact/reference solution. We denote the mesh size vector $\vec{h}$ simply by h if $h_j = h$ for $j = 1,\ldots,d$. The algorithm has been implemented in FORTRAN, and all reported timing results are obtained using a single 2.60GHz Intel(R) Core(TM) i7-6660U CPU with 4MB cache with the Intel compiler ifort and optimization level -O3.

4.1. Coulomb potentials.

EXAMPLE 1. *The 2D Coulomb potential* ($U(r) = -\frac{1}{2\pi}\ln\ r$).

Case I: We first test the method with an isotropic Gaussian source $\rho(\mathbf{x}) := e^{-|\mathbf{x}|^2/\sigma^2}$ with $\sigma > 0$. The corresponding potential is given by

$$\phi(\mathbf{x}) = -\frac{\sigma^2}{4}\left[\mathrm{E}_1\left(\frac{|\mathbf{x}|^2}{\sigma^2}\right) + 2\ln(|\mathbf{x}|)\right], \tag{4.2}$$

where $\mathrm{E}_1(r) := \int_r^\infty t^{-1}e^{-t}dt$ for $r > 0$ is the exponential integral function [39].
Case II: We next consider an anisotropic Gaussian source $\rho(\mathbf{x})$ generated by taking the Laplacian of the potential $\phi(\mathbf{x}) = e^{-\frac{x^2}{\sigma^2}-\frac{y^2}{\alpha^2}}, \alpha, \sigma > 0$ as follows:

$$\rho(\mathbf{x}) = -\Delta\phi(\mathbf{x}) = \phi(\mathbf{x})\left(-\frac{4x^2}{\sigma^4} - \frac{4y^2}{\alpha^4} + \frac{2}{\alpha^2} + \frac{2}{\sigma^2}\right). \tag{4.3}$$

Table 4.1 shows the errors for the 2D Coulomb potential with various mesh sizes in Example 1 on $\mathbf{R}_{10\boldsymbol{\gamma}}$ with $\boldsymbol{\gamma} = (1, \gamma)$. For *Case I*, we set $\sigma = \sqrt{1.2}$, $\gamma = 1$ and the mesh size $h_x = h_y = h$, and for *Case II* we set $\sigma = 1.2, \alpha = \gamma\ \sigma$ and $\vec{h} = \frac{1}{4}(1, \gamma)^T$. The saturated accuracy of Case I comes from the Gaussian-sum approximation of the kernel, which could certainly be further improved with more accurate Gaussian-sum approximations if needed.

TABLE 4.1
Errors (E) for the 2D Poisson potential in Example 1 on $\boldsymbol{R}_{10\boldsymbol{\gamma}}$. For Case I, $\sigma = \sqrt{1.2}$, $\gamma = 1$ *and we use a uniform mesh with N points. For* Case II, $\sigma = 1.2, \alpha = \gamma\ \sigma$ *and we fix* $\vec{h} = \frac{1}{4}(1, \gamma)^T$, *corresponding to an anisotropic grid with* $N = 80 \times 80$ *points.*

Case I	$N = 10^2$	$N = 20^2$	$N = 40^2$	$N = 80^2$	$N = 160^2$
E	2.180E-01	9.624E-04	5.134E-09	5.854E-11	5.853E-11
Case II	$\gamma = 1$	$\gamma = 1/2$	$\gamma = 1/4$	$\gamma = 1/8$	$\gamma = 1/16$
E	6.767E-13	3.913E-13	2.816E-13	2.299E-13	2.701E-13

EXAMPLE 2. *The 3D Coulomb potential restricted to a plane* ($U(r) = \frac{1}{2\pi}\frac{1}{r}$).

We next consider the anisotropic source $\rho(\mathbf{x}) = e^{-(x^2+y^2/\gamma^2)/\sigma^2}$ with $\sigma > 0$ and $\gamma \le 1$. The Coulomb potential with targets restricted to the xy-plane is given analytically [6] by

$$\phi(\mathbf{x}) = \frac{\gamma\ \sigma}{\sqrt{\pi}}\int_0^\infty \frac{e^{-\frac{x^2}{\sigma^2(t^2+1)}}e^{-\frac{y^2}{\sigma^2(t^2+\gamma^2)}}}{\sqrt{t^2+1}\sqrt{t^2+\gamma^2}}dt. \tag{4.4}$$

A reference solution is obtained by applying adaptive Gauss–Kronrod quadrature to the above integral and requesting double precision accuracy. The Fourier transform of the isotropically truncated Coulomb kernel with a ball B_D of radius D is given as follows

$$\begin{aligned}\widehat{U}_B(\mathbf{k}) &= 2\pi\int_0^D J_0(kr)U(r)rdr = \int_0^D J_0(kr)dr \\ &= \frac{D}{2}\big(\pi\, J_1(kD)\,\mathrm{SH}_0(kD) + J_0(kD)\ (2 - \pi\,\mathrm{SH}_1(kD))\big), \quad k = |\mathbf{k}|,\end{aligned} \tag{4.5}$$

where J_0, J_1 are Bessel functions of the first kind with index 0 and 1, and $\mathrm{SH}_0, \mathrm{SH}_1$ are Struve functions of order 0 and 1, respectively [39].

A comparison with the TKM for this Coulomb potential is presented in Table 4.2 on the domain $\mathbf{R}_{12\boldsymbol{\gamma}}$ for various anisotropic vectors $\boldsymbol{\gamma} = (1, \gamma)^T$ and mesh size vectors $\vec{h} = \frac{1}{4}\boldsymbol{\gamma}$. From Table 4.2 one can see clearly that both methods are spectrally accurate, that the minimum storage required for the TKM depends linearly on the anisotropy factor $\gamma_f = \gamma$, but that the storage of the ATKM remains unchanged with respect to γ_f.

TABLE 4.2
Comparison of the ATKM and the TKM for the Coulomb potential in Example 2 on $\boldsymbol{R}_{L\boldsymbol{\gamma}}$: $L = 12, \sigma = 1.5, \vec{h} = \frac{1}{4}(1, \gamma)^T$. N denotes the number of grid points and E denotes the error.

		$\gamma = 1$	$\gamma = 1/2$	$\gamma = 1/4$	$\gamma = 1/8$	$\gamma = 1/16$
ATKM	N	192×192	192×192	192×192	192×192	192×192
	E	1.004E-15	9.738E-16	7.589E-16	1.0572E-15	3.247E-15
TKM	N	192×192	192×384	192×768	192×1536	192×3072
	E	3.353E-16	3.661E-16	3.798E-16	4.531E-16	3.562E-15

EXAMPLE 3. *The 3D Coulomb potential ($U(r) = \frac{1}{4\pi}\frac{1}{r}$).*

Let

$$\rho_{\mathbf{0}}(\mathbf{x}) := e^{-(x^2+y^2+z^2/\gamma_3^2)/\sigma^2}$$

with $\gamma_3 \leq 1$ be an anisotropic Gaussian source distribution. For

$$\rho(\mathbf{x}) = \rho_{\mathbf{0}}(\mathbf{x}) + \rho_{\mathbf{0}}(\mathbf{x} - \mathbf{x}_0),$$

the corresponding potential is

$$\phi(\mathbf{x}) = \phi_{\mathbf{0}}(\mathbf{x}) + \phi_{\mathbf{0}}(\mathbf{x} - \mathbf{x}_0).$$

where

$$\phi_{\mathbf{0}}(\mathbf{x}) = \frac{\gamma_3\sigma^2}{4}\int_0^\infty \frac{e^{-\frac{x^2+y^2}{\sigma^2(t+1)}} e^{-\frac{z^2}{\sigma^2(t+\gamma_3^2)}}}{(t+1)\sqrt{t+\gamma_3^2}}dt, \qquad \mathbf{x} \in \mathbb{R}^3. \tag{4.6}$$

We let $\mathbf{x}_0 = (2, 2, 0)^T$, requiring a 256^3 uniform mesh for resolution to double precision accuracy.

The error and timing results for the ATKM are presented in Table 4.3. Here, T_{precomp} is the time for the precomputation of $\widehat{U}_R$, and T_{FFT} is the time of the FFT. The cut-off parameter δ and the number of Gaussian S are also shown.

To compare the performance of the TKM and the ATKM, we consider the single anisotropy Gaussian bump $\rho_{\mathbf{0}}(\mathbf{x}) = e^{-(x^2+y^2+z^2/\gamma_3^2)/\sigma^2}$ and determine the total number of grid points N needed to achieve the indicated error E in Table 4.4. Figure 4.1 shows the CPU time in seconds for the TKM and the ATKM as a function of the anisotropy factor. Clearly, the ATKM is capable of accurate evaluation of the Coulomb potential without increasing the storage and computation costs as the anisotropy factor increases. The TKM can be made as accurate as the ATKM, but the storage and computation costs grow linearly with the anisotropy factor.

TABLE 4.3
Error and timing results of the ATKM for the 3D Coulomb potential (Example 3) on $\boldsymbol{R}_{L\boldsymbol{\gamma}}$. Here, $L = 16$, $\sigma = 2$, $\boldsymbol{\gamma} = (1, 1, \gamma_3)$, $\vec{h} = \frac{1}{4}\boldsymbol{\gamma}$. N denotes the number of grid points and E denotes the error. $T_{precomp}$ is the time for precomputing $\widehat{U}_R$, T_{FFT} is the FFT time. δ is the cut-off parameter and S is the number of Gaussian S used in the kernel approximation.

γ_3	N	E	T_{precomp}	T_{FFT}	δ	S
1	256^3	6.589E-16	3.685	0.8586	4.974E-07	198
1/2	256^3	6.631E-16	3.831	0.8796	2.487E-07	205
1/4	256^3	8.083E-16	3.739	0.8211	1.243E-07	213
1/8	256^3	7.630E-16	3.856	0.8216	6.217E-08	220

TABLE 4.4
Comparison with the TKM for the 3D Coulomb potential with anisotropic Gaussian density (Example 3): $\rho(\boldsymbol{x}) = e^{-(x^2+y^2+z^2/\gamma_3^2)/\sigma^2}$ on $\boldsymbol{R}_{L\boldsymbol{\gamma}}$: $L = 12$, $\sigma = 2$, $\boldsymbol{\gamma} = (1, 1, \gamma_3)^T$ and $\vec{h} = \frac{1}{2}\boldsymbol{\gamma}$. N denotes the number of grid points and E denotes the error.

		$\gamma_3 = 1$	$\gamma_3 = 1/2$	$\gamma_3 = 1/4$	$\gamma_3 = 1/8$	$\gamma_3 = 1/16$
ATKM	N	96^3	96^3	96^3	96^3	96^3
	E	3.522E-15	6.932E-15	1.466E-14	3.021E-14	6.150E-14
TKM	N	96^3	$96^3 \times 2$	$96^3 \times 4$	$96^3 \times 8$	$96^3 \times 16$
	E	3.501E-15	6.957E-15	1.454E-14	2.995E-14	6.200E-14

4.2. Yukawa potentials.

EXAMPLE 4. *The 2D Yukawa potential ($U(r) = \frac{1}{2\pi} K_0(\lambda r)$).*

Given a potential $\phi(\mathbf{x}) = e^{-\frac{x^2}{\sigma^2} - \frac{y^2}{\delta^2}}$, we define the corresponding density $\rho(\mathbf{x})$ by

$$\rho(\mathbf{x}) = \left(\frac{-4x^2\delta^4 - 4\,y^2\sigma^4 + 2\sigma^2\delta^4 + 2\delta^2\sigma^4}{\sigma^4\delta^4} + \lambda^2 \right) \phi(\mathbf{x})\,, \tag{4.7}$$

so that

$$(-\Delta + \lambda^2)\phi(\mathbf{x}) = \rho(\mathbf{x}).$$

We compute the convolution $(U * \rho)[\mathbf{x}]$ using the ATKM to obtain an approximate solution $\phi_{\vec{h}}$. For this, the Fourier transform of the isotropically truncated 2D Yukawa kernel in a ball B_D of radius D is

$$\widehat{U}_B(k) = \frac{1}{k^2 + \lambda^2} \left[1 + k\,D J_1(kD) K_0(\lambda D) - D\lambda J_0(k\,D) K_1(\lambda\,D) \right], \tag{4.8}$$

where $K_0(r)$ and $K_1(r)$ are modified Bessel functions of the second kind with order 0 and 1, respectively. In Table 4.5, we present results for the ATKM. As above, the cost remains independent of the anisotropy, whereas it grows linearly with γ_f for the TKM.

EXAMPLE 5. *3D Yukawa potential ($U(r) = \frac{e^{-\lambda r}}{4\pi r}$).*

Case I: We consider the isotropic Gaussian source $\rho_{\mathbf{0}}(\mathbf{x}) = e^{-|\mathbf{x}|^2/2/\sigma^2}, \sigma > 0$, which generates the exact potential [12]

$$\phi_{\mathbf{0}}(\mathbf{x}) = \sqrt{2}(\sqrt{\pi}\sigma)^3 \frac{e^{-\lambda r + \frac{\lambda^2\sigma^2}{2}}}{4\pi r} \left[\operatorname{erfc}\left(-\frac{r}{\sqrt{2}\sigma} + \frac{\lambda\sigma}{\sqrt{2}} \right) - e^{2\lambda r} \operatorname{erfc}\left(\frac{r}{\sqrt{2}\sigma} + \frac{\lambda\sigma}{\sqrt{2}} \right) \right],$$

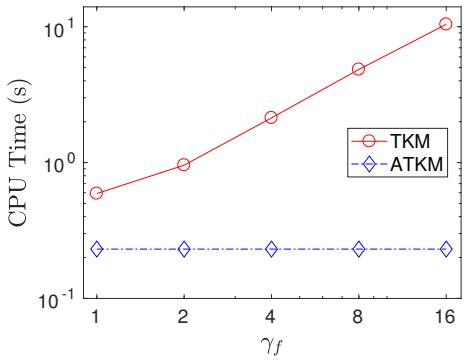

FIG. 4.1. *Timing results for the TKM and the ATKM as a function of the anisotropy factor. The data corresponds to experiments carried out for the 3D Coulomb potential (Example 3), described in Table 4.4.*

TABLE 4.5

Comparison with the TKM for the 2D Yukawa potential (Example 4) on $\boldsymbol{R}_{L\boldsymbol{\gamma}}$: $L = 12$, $\lambda = 1$, $\sigma = \sqrt{1.5}$, $\delta = \gamma\sigma$, $\vec{h} = h\boldsymbol{\gamma} = \frac{1}{4}(1,\gamma)^T$. N denotes the number of grid points and E denotes the error.

		$\gamma = 1$	$\gamma = 1/2$	$\gamma = 1/4$	$\gamma = 1/8$	$\gamma = 1/16$
ATKM	N	192×192	192×192	192×192	192×192	192×192
	E	4.495E-16	3.343E-16	1.615E-16	2.259E-16	6.183E-16
TKM	N	192×192	192×384	192×768	192×1536	192×3072
	E	2.221E-16	2.245E-16	4.463E-16	8.882E-16	1.999E-15

where $\mathrm{erfc}(x) = 1 - \frac{2}{\sqrt{\pi}}\int_0^x e^{-t^2}dt$ is the complementary error function. To add some complexity to the calculation, we consider a density that is composed of multiple such Gaussians:

$$\rho(\mathbf{x}) = \sum_{i,j,k\in\{0,1\}} \rho_{\mathbf{0}}(\mathbf{x} - \mathbf{x}_{ijk}),$$

and the potential is given as $\phi(\mathbf{x}) = \sum_{i,j,k\in\{0,1\}} \phi_{\mathbf{0}}(\mathbf{x}-\mathbf{x}_{ijk})$, where $\mathbf{x}_{ijk} = (2^i, 2^j, 3^k)^T$ are shifted centers.

Case II: Let $\phi_(\mathbf{x})$ be given by the anisotropic Gaussian potential

$$\phi_{\mathbf{0}}(\mathbf{x}) = e^{-(x^2/\gamma_1^2 + y^2/\gamma_2^2 + z^2/\gamma_3^2)/\sigma^2},\ 0 < \gamma_j \le 1,$$

and let

$$\rho_{\mathbf{0}}(\mathbf{x}) = -\left(\frac{4x^2}{\gamma_1^4\sigma^4} - \frac{2}{\gamma_1^2\sigma^2} + \frac{4y^2}{\gamma_2^4\sigma^4} - \frac{2}{\gamma_2^2\sigma^2} + \frac{4z^2}{\gamma_3^4\sigma^4} - \frac{2}{\gamma_3^2\sigma^2} - \lambda^2\right)\phi_{\mathbf{0}}(\mathbf{x})\,.$$

Letting $\phi(\mathbf{x}) = \phi_{\mathbf{0}}(\mathbf{x}) + \phi_{\mathbf{0}}(\mathbf{x} - \mathbf{x}_0)$, it is easy to verify that

$$(-\Delta + \lambda^2)\phi(\mathbf{x}) = \rho(\mathbf{x}),$$

where $\rho(\mathbf{x}) = \rho_{\mathbf{0}}(\mathbf{x}) + \rho_{\mathbf{0}}(\mathbf{x} - \mathbf{x}_0)$. We compute the convolution $(U * \rho)[\mathbf{x}]$ using the ATKM to obtain an approximate solution $\phi_{\vec{h}}$ for $\mathbf{x}_0 = (\frac{16}{3}, \frac{8}{3}, 0)^T$.

Table 4.6 shows the errors and timing results for the 3D Yukawa potentials in Example 5.

TABLE 4.6

Error and timing results of the ATKM for the 3D Yukawa potential (Example 5) on $\boldsymbol{R}_{L\boldsymbol{\gamma}}$ with $\sigma = \frac{1}{4}$. Case I*: $L = 12, \vec{h} = h(1,1,1)^T$;* Case II*:$L = 8, \vec{h} = \frac{1}{16}(1, \frac{1}{2}, \gamma_3)^T$. N denotes the number of grid points and E denotes the error. $T_{precomp}$ is the time for precomputing $\widehat{U}_R$, T_{FFT} is the FFT time. δ is the cut-off parameter and S is the number of Gaussian S used in the kernel approximation.*

Case I	N	E	T_{precomp}	T_{FFT}	δ	S
$h = 1/2$	96^3	0.119	0.080	0.027	1.326E-06	104
$h = 1/4$	192^3	1.849E-04	0.814	0.297	6.631E-07	109
$h = 1/8$	384^3	2.996E-12	6.759	2.789	3.316E-07	112
$h = 1/16$	768^3	7.990E-16	41.66	26.32	1.658E-07	116
Case II	N	E	T_{precomp}	T_{FFT}	δ	S
$\gamma_3 = 1$	512^3	1.403E-15	13.98	10.08	1.243E-07	124
$\gamma_3 = 1/2$	512^3	7.400E-16	17.92	9.651	1.243E-07	124
$\gamma_3 = 1/4$	512^3	2.296E-15	15.75	10.06	6.217E-08	129
$\gamma_3 = 1/8$	512^3	5.161E-15	18.07	9.677	3.108E-08	134
$\gamma_3 = 1/16$	512^3	4.502E-15	16.93	9.866	1.554E-08	139

4.3. Biharmonic potentials.

EXAMPLE 6. *The 2D biharmonic potential ($U(r) = -\frac{1}{8\pi}\, r^2(\log(r) - 1)$).*

Case I: We consider the isotropic Gaussian source

$$\rho(\mathbf{x}) = \frac{1}{2\pi\sigma^2}\, e^{-\frac{|\mathbf{x}|^2}{2\sigma^2}}, \qquad \mathbf{x} \in \mathbb{R}^2,$$

which generates the exact potential

$$\phi(\mathbf{x}) = \frac{1}{8\pi}\left(r^2 + e^{-\frac{r^2}{2\sigma^2}}\sigma^2\right) + \frac{1}{16\pi}\left(r^2 + 2\sigma^2\right)\left(\text{Ei}\left(-\frac{r^2}{2\sigma^2}\right) - 2\log(r)\right),$$

where $r = |\mathbf{x}|$ and $\text{Ei}(x) := \int_{-\infty}^{x} \frac{e^s}{s} ds$ is the exponential integral [39].
Case II: Let the exact solution $\phi(\mathbf{x})$ be given by the anisotropic Gaussian potential $\phi(\mathbf{x}) = e^{-(x^2/\gamma_1^2 + y^2/\gamma_2^2)/\sigma^2}$, $0 < \gamma_j \leq 1, j = 1, 2$, and let

$$\rho(\mathbf{x}) = -\Delta^2 \phi(\mathbf{x}).$$

Numerical results are presented in Table 4.7. Spectral convergence is evident until the error in the kernel approximation using a sum of Gaussians begins to dominate.

TABLE 4.7

Errors (E) for the 2D biharmonic potential in Example 6 on $\boldsymbol{R}_{L\boldsymbol{\gamma}}$. For Case I*, $L = 12, \sigma = \sqrt{1.2}$ and we use a uniform mesh with N points. For* Case II*, $L = 10, \sigma = 1.2, \boldsymbol{\gamma} = (1, \gamma)^T$ and we fix $\vec{h} = \frac{1}{4}(1, \gamma)^T$, corresponding to an anisotropic grid with $N = 80 \times 80$ points.*

Case I	$N = 48^2$	$N = 96^2$	$N = 128^2$	$N = 256^2$
E	9.333E-03	7.516E-07	3.172E-11	3.172E-11
Case II	$\gamma = 1$	$\gamma = 1/2$	$\gamma = 1/4$	$\gamma = 1/8$
E	1.604E-10	5.305E-10	1.767E-09	8.482E-09

EXAMPLE 7. *The 3D biharmonic potential ($U(r) = \frac{r}{8\pi}$).*

Case I: We consider the isotropic Gaussian source

$$\rho(\mathbf{x}) = \frac{1}{(2\pi)^{3/2}\sigma^3} e^{-\frac{|\mathbf{x}|^2}{2\sigma^2}}, \qquad \mathbf{x} \in \mathbb{R}^3,$$

which generates the exact potential [12]

$$\phi(\mathbf{x}) = \frac{1}{8\pi}\left(\mathrm{Erf}\left(\frac{\mathrm{r}}{\sqrt{2}\sigma}\right)\left(\frac{\sigma^2}{\mathrm{r}} + \mathrm{r}\right) + \sigma\sqrt{\frac{2}{\pi}}\,\mathrm{e}^{-\frac{\mathrm{r}^2}{2\sigma^2}}\right), \quad r = |\mathbf{x}|.$$

Case II: Let $\phi(\mathbf{x})$ be given by the anisotropic Gaussian potential

$$\phi(\mathbf{x}) = e^{-(x^2/\gamma_1^2 + y^2/\gamma_2^2 + z^2/\gamma_3^2)/\sigma^2}, \ 0 < \gamma_j \le 1,$$

and let

$$\rho(\mathbf{x}) = -\Delta^2\phi(\mathbf{x}).$$

We compute the convolution $(U * \rho)[\mathbf{x}]$ using the ATKM to obtain an approximate solution $\phi_{\vec{h}}$.

Table 4.8 presents the errors and timing results for the 3D biharmonic potentials in Example 7.

TABLE 4.8

Error and timing results of the 3D biharmonic potential (Example 7) on $\boldsymbol{R}_{L\boldsymbol{\gamma}}$ with $\sigma = \sqrt{1.2}$. Case I*: $L = 12, \boldsymbol{\gamma} = (1,1,1)^T, \vec{h} = h\boldsymbol{\gamma}$:* Case II*: $L = 10, \boldsymbol{\gamma} = (1, \frac{1}{4}, \gamma_3)^T$ and $\vec{h} = \frac{1}{4}\boldsymbol{\gamma}$. N denotes the number of grid points and E denotes the error. $T_{precomp}$ is the time for precomputing $\widehat{U}_R$, T_{FFT} is the FFT time. δ is the cut-off parameter and S is the number of Gaussian S used in the kernel approximation.*

Case I	N	E	T_{precomp}	T_{FFT}	δ	S
$h = 1$	48^3	1.585E-02	9.700E-03	5.000E-04	5.305E-06	199
$h = 1/2$	96^3	5.962E-07	4.070E-02	2.900E-03	2.653E-06	199
$h = 1/4$	192^3	1.031E-11	2.373E-01	2.800E-02	1.326E-06	203
$h = 1/8$	384^3	1.701E-11	1.809	3.356E-01	6.631E-07	213
Case II	N	E	T_{precomp}	T_{FFT}	δ	S
$\gamma_3 = 1$	160^3	5.499E-12	1.057	0.176	1.989E-07	213
$\gamma_3 = 1/2$	160^3	3.692E-12	1.070	0.168	1.989E-07	213
$\gamma_3 = 1/4$	160^3	3.260E-12	1.060	0.184	1.989E-07	213
$\gamma_3 = 1/8$	160^3	1.873E-11	1.064	0.169	9.947E-08	213

4.4. Application to anisotropic layered media. We consider the transmission problem (see Figure 4.2)

$$-\nabla \cdot (\varepsilon_i \nabla\phi) = f_i, \quad i = 1, 2, \tag{4.9}$$

subject to continuity conditions at the interface, i.e., at the xy-plane ($z = 0$)

$$\begin{aligned} [\phi] &:= \phi(x, y, 0+) - \phi(x, y, 0-) = 0, \\ [\varepsilon\partial_{\mathbf{n}}\phi] &:= \varepsilon_1\phi_z(x, y, 0+) - \varepsilon_2\phi_z(x, y, 0-) = 0, \end{aligned} \tag{4.10}$$

where ε_i $(i = 1, 2)$ are constants and the source terms f_1, f_2 are given smooth and rapidly decaying functions with (numerical) compact support in regions I and II, respectively. We will consider source densities that are strongly anisotropic, in the sense

that their extent in the z-direction is very small compared to their extents in the x and y directions. One such example density is $f_1(\mathbf{x}) = e^{-\left((x-x_0)^2+(y-y_0)^2+(z-z_0)^2/\eta^2\right)/\sigma^2}$ with $\eta \ll 1$.

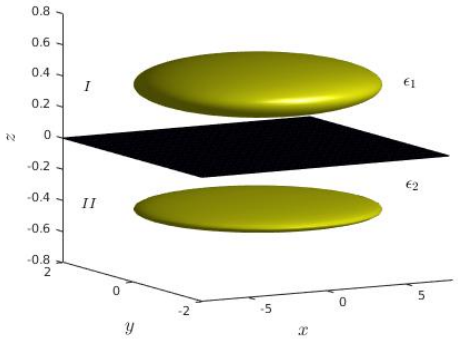

FIG. 4.2. *Schematic of the anisotropic layered problem.*

We first decompose ϕ into two parts using standard potential theory. That is, $\phi = \phi^F + \phi^S$, where ϕ^F is the volume potential due to the inhomogeneous source terms

$$\phi^F(\mathbf{x}) = \begin{cases} \frac{1}{4\pi|\mathbf{x}|} * \frac{f_1}{\varepsilon_1}, & \mathbf{x} \in I, \\ \frac{1}{4\pi|\mathbf{x}|} * \frac{f_2}{\varepsilon_2}, & \mathbf{x} \in II. \end{cases} \tag{4.11}$$

We apply the ATKM to calculate ϕ^F on a uniform grid. In order for ϕ to satisfy the continuity conditions above, we let ϕ^S denote a correction term which satisfies the Laplace equation in both the upper and lower half-spaces with suitable decay conditions at infinity. It is well-known that ϕ^S can be represented using a "Sommerfeld-type" integral [38] of the form

$$\phi^S(\mathbf{x}) = \begin{cases} \frac{1}{(2\pi)^2} \int_0^\infty e^{-kz} dk \int_0^{2\pi} M_1(k,\beta) e^{ik(x\cos\beta + y\sin\beta)} d\beta, & z > 0, \\ \frac{1}{(2\pi)^2} \int_0^\infty e^{kz} dk \int_0^{2\pi} M_2(k,\beta) e^{ik(x\cos\beta + y\sin\beta)} d\beta, & z < 0, \end{cases}$$

Here, M_1 and M_2 are unknown densities to be determined.

Direct application of (4.10) leads to a 2×2 linear system for each point (k, β).

$$\begin{cases} M_1 - M_2 = k\, g_1, \\ \varepsilon_1 M_1 + \varepsilon_2 M_2 = -g_2, \end{cases} \Longrightarrow \begin{cases} M_1 = \frac{1}{\varepsilon_1+\varepsilon_2}(\varepsilon_2 k\, g_1 - g_2), \\ M_2 = \frac{1}{\varepsilon_1+\varepsilon_2}(-\varepsilon_1 k\, g_1 - g_2), \end{cases} \tag{4.12}$$

where

$$g_1(k,\beta) := -\frac{1}{2\pi} \int_{\mathbb{R}} \frac{\widehat{f_1}(k,\beta,k_3)/\varepsilon_1 - \widehat{f_2}(k,\beta,k_3)/\varepsilon_2}{k^2 + k_3^2} dk_3, \tag{4.13}$$

$$g_2(k,\beta) := -\frac{1}{2\pi} \int_{\mathbb{R}} \frac{\left(\widehat{f_1}(k,\beta,k_3) - \widehat{f_2}(k,\beta,k_3)\right) ik_3}{k^2 + k_3^2} dk_3, \tag{4.14}$$

using cylindrical coordinates (k, β, k_3).

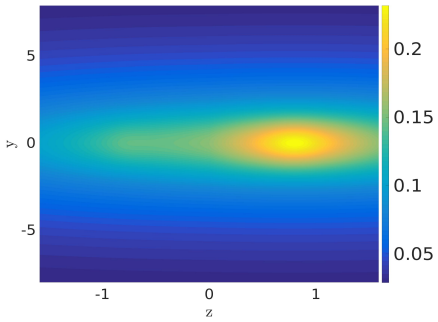

FIG. 4.3. *Potential in the plane $x = 0$,i.e., $\phi(0, y, z)$.*

For each (k, β), we compute kg_1 and g_2 using adaptive Gauss-Kronrod quadrature. Once M_1 and M_2 are obtained from (4.12), $\phi^S(\mathbf{x})$ is then evaluated using the NUFFT-based method of [5, 27].

In our example, we set $\varepsilon_1 = 1$, $\varepsilon_2 = 2$, and

$$f_i(\mathbf{x}) = e^{-\frac{(x-x_i)^2}{\sigma_{i,x}^2} - \frac{(y-y_i)^2}{\sigma_{i,y}^2} - \frac{(z-z_i)^2}{\sigma_{i,z}^2}}, \quad i = 1, 2,$$

with $\vec{\sigma}_1 = (2.5, 1.1, 0.2)^T$, $\vec{\sigma}_2 = (2.5, 1.1, 0.1)^T$ and the centers $\mathbf{x}_1 = (x_1, y_1, z_1)^T = (0, 0, 0.8)^T$, $\mathbf{x}_2 = (0, 0, -0.8)^T$. The computational domain is chosen to be $[-8, 8]^2 \times [0, 1.6]$ for region I and $[-8, 8]^2 \times [-1.6, 0]$ for region II, respectively. The mesh sizes are set to be $h_x = h_y = \frac{1}{8}$ and $h_z = \frac{1}{80}$ in both regions. In Figure 4.3, we plot the potential as a function of y and z in the plane $x = 0$. Numerical convergence tests indicate that at least 10 digits of accuracy are obtained with a $128 \times 128 \times 256$ grid.

5. Conclusion. We have developed a new method – the anisotropic truncated kernel method (ATKM) for computing nonlocal potentials that are convolutions of a radially symmetric kernel with a smooth and rapidly decaying source density. When the density has compact support on an *anisotropic* rectangular box $\mathbf{R}_{L\boldsymbol{\gamma}}$, the kernel is truncated on a rectangular box $\mathbf{R}_{2L\boldsymbol{\gamma}}$ that doubles the length of each side. The potential is then computed via the FFT with an optimal zero-padding factor (2^d) for problems in d dimensions. The method is a useful extension of the isotropic kernel truncation method in [49], since it avoids excessive zero-padding for highly anisotropic problems and reduces the cost by a factor of γ_f (see Definition (1.5)).

A fast algorithm is required to obtain the Fourier transform of the anisotropically truncated kernel. For this, we used a sum-of-Gaussians approximation of the kernel away from the origin plus a local correction to handle the singularity at the origin. The Gaussian-sum approximation is obtained either via a spectral discretization of an integral representation of the kernel (when available), or via a black-box algorithm in the general case. The algorithm applies to nonoscillatory kernels, including many of the kernels encountered in mathematical physics and engineering. We are currently investigating oscillatory problems such as the Helmholtz equation, and will report our findings at a later date.

REFERENCES

[1] J. C. Aguilar and Y. Chen, *High-Order Corrected Trapezoidal Quadrature Rules for Functions with a Logarithmic Singularity in 2-D*, Comput. Math. Appl., 44 (2002), pp. 1031–1039.

[2] J. C. Aguilar and Y. Chen, *High-order corrected trapezoidal quadrature rules for the coulomb potential in three dimensions*, Comput. Math. Appl., 49 (2005), pp. 625–631.

[3] W. Bao, Y. Cai, and H. Wang, *Efficient numerical methods for computing ground states and dynamics of dipolar Bose-Einstein condensates*, J. Comput. Phys., 229 (2010), pp. 7874–7892.

[4] W. Bao, H. Jian, N. Mauser, and Y. Zhang, *Dimension reduction of the Schrödinger equation with Coulomb and anisotropic confining potentials*, SIAM J. Appl. Math., 73 (2010), pp. 7874–7892.

[5] W. Bao, S. Jiang, Q. Tang, and Y. Zhang, *Computing the ground state and dynamics of the nonlinear Schrödinger equation with nonlocal interactions via the nonuniform FFT*, J. Comput. Phys., 296 (2015), pp. 72–89.

[6] W. Bao, Q. Tang, and Y. Zhang, *Accurate and efficient numerical methods for computing ground states and dynamics of dipolar Bose-Einstein condensates via the nonuniform FFT*, Comm. Comput. Phys., 19 (2016), pp. 1141—1166.

[7] J. T. Beale and M.-C. Lai, *A method for computing nearly singular integrals*, SIAM J. Numer. Anal, 38 (2001), pp. 1902–25.

[8] C. Bertoglio and B. N. Khoromskij, *Low-rank quadrature-based tensor approximation of the Galerkin projected Newton/Yukawa kernels*, Comput. Phys. Comm., 183 (2012), pp. 904—912.

[9] G. Beylkin, C. Kurzc, and L. Monzón, *Fast convolution with the free space Helmholtz Green's function*, J. Comput. Phys., 228 (2009), pp. 2770–2791.

[10] G. Beylkin and L. Monzón, *Approximation by exponential sums*, Appl. Comput. Harmon. Anal., 19 (2005), pp. 17–48.

[11] G. Beylkin and L. Monzón, *Approximation by exponential sums revisited*, Appl. Comput. Harmon. Anal., 28 (2010), pp. 131–149.

[12] A. Cerioni, L. Genovese, A. Mirone, and V. Sole, *Efficient and accurate solver of the three-dimensional screened and unscreened Poisson's equation with generic boundary conditions*, J. Chem. Phys., 137 (2012), p. 134108.

[13] T. Darden, D. York, and L. Pedersen, *Particle mesh ewald - an $o(n \log n)$ method for Ewald sums in large systems*, J. Chem. Phys., 98 (1993), pp. 10089–10092.

[14] R. Duan and V. Rokhlin, *High-order quadratures for the solution of scattering problems in two dimensions*, J. Comput. Phys., 228 (2009), pp. 2152–2174, doi:10.1016/j.jcp.2008.11.033.

[15] A. Dutt and V. Rokhlin, *Fast Fourier transforms for nonequispaced data*, SIAM J. Sci. Comput., 14 (1993), pp. 1368–1393.

[16] F. Ethridge and L. Greengard, *A New Fast-Multipole Accelerated Poisson Solver in Two Dimensions*, SIAM J. Sci. Comput., 23 (2001), pp. 741–760.

[17] L. Exl, N. Mauser, and Y. Zhang, *Accurate and efficient computation of nonlocal potentials based on Gaussian-sum approximation*, J. Comput. Phys., 327 (2016), pp. 629–642.

[18] L. Füsti-Molnar and P. Pulay, *Accurate molecular integrals and energies using combined plane wave and Gaussian basis sets in molecular electronic structure theory*, J. Chem. Phys., 116 (2002), p. 7795.

[19] W. Gautschi, *Efficient computation of the complex error function*, SIAM J. Numer. Anal., 7 (1970), pp. 187–198.

[20] L. Genovese, T. Deutsch, and S. Goedecker, *Efficient and accurate three-dimensional Poisson solver for surface problems*, J. Chem. Phys., 127 (2007), p. 054704.

[21] L. Genovese, T. Deutsch, A. Neelov, S. Goedecker, and G. Beylkin, *Efficient solution of Poisson equation with free boundary conditions*, J. Chem. Phys., 125 (2006), p. 074105.

[22] K. Glover, *All optimal Hankel-norm approximations of linear multivariable systems and their l^∞-error bounds*, Int. J. Control, 39 (1984), pp. 1115–1193.

[23] J. Goodman, T. Y. Hou, and J. Lowengrub, *The convergence of the point vortex method for the 2-D Euler equations*, Commun. Pur. Appl. Math., 43 (1990), pp. 415–430.

[24] L. Greengard and J. Y. Lee, *Accelerating the nonuniform fast Fourier transform*, SIAM Rev., 46 (2004), pp. 443–454.

[25] W. Hackbusch and B. Khoromskij, *Low-rank Kronecker-product approximation to multi-dimensional nonlocal operators. Part I. Separable approximation of multi-variate functions*, Computing, 76 (2006), pp. 177–202.

[26] M. R. Jarvis, I. D. White, R. W. Godby, M. C. Payne, and A. Rubio, *Supercell technique for total-energy calculations of finite charged and polar systems*, Phys. Rev. B, 56 (1997), p. 14972.

[27] S. Jiang, L. Greengard, and W. Bao, *Fast and accurate evaluation of nonlocal Coulomb and dipole-dipole interactions via the nonuniform FFT*, SIAM J. Sci. Comput., 36 (2014), pp. B777–B794.
[28] S. Jiang and Y. Zhang, *A black-box algorithm for efficient and accurate sum-of-exponential approximation of certain class of functions on an interval.* in preparation, 2018.
[29] S. G. Johnson, *Faddeeva Package.* http://ab-initio.mit.edu/wiki/index.php/Faddeeva_Package, 2012.
[30] H. Langston, L. Greengard, and D. Zorin, *A free-space adaptive fmm-based pde solver in three dimensions*, Comm. Appl. Math. and Comp. Sci., 6 (2011), pp. 79–122.
[31] H. Lee, T. Darden, and L. Pedersen, *Accurate crystal molecular dynamics simulations using Particle-Mesh-Ewald*, Chemical Physics Letters, 243 (1995), pp. 229–235.
[32] D. Lindbo and A.-K. Tornberg, *Spectral accuracy in fast Ewald-based methods for particle simulations*, J. Comput. Phys., 230 (2011), pp. 8744–8761.
[33] J. Lowengrub, M. Shelley, and B. Merriman, *High-order and efficient methods for the vorticity formulation of the Euler equations*, SIAM J. Sci. Comput., 14 (1993), pp. 1107–1142.
[34] D. Malhotra and G. Biros, *A parallel kernel independent fmm for particle and volume potentials*, Commun. Comput. Phys., 18 (2015), pp. 808–830.
[35] G. Martyna and M. Tuckerman, *A reciprocal space based method for treating long range interactions in ab initio and force-field-based calculations in clusters*, J. Chem. Phys., 110 (1999), pp. 2810–2821.
[36] N. Mauser, H. Stimming, and Y. Zhang, *A novel nonlocal potential solver based on nonuniform FFT for efficient simulation of the Davey-Stewartson equations*, ESAIM: Math. Model. Numer. Anal., 51 (2017), pp. 1527–1538.
[37] P. Mccorquodale, P. Colella, G. T. Balls, and S. B. Baden, *A scalable parallel poisson solver in three dimensions with infinite-domain boundary conditions*, in In 7th International Workshop on High Performance Scientific and Engineering Computing, 2005, pp. 814–822.
[38] P. Morse and H. Feshbach, *Methods of Theoretical Physics*, McGraw-Hill, New York, NY, 1953.
[39] F. W. J. Olver, D. W. Lozier, R. F. Boisvert, and C. W. Clark, eds., *NIST Handbook of Mathematical Functions*, Cambridge University Press, May 2010, http://dlmf.nist.gov.
[40] J. Phillips and J. White, *A Precorrected-FFT method for capacitance extraction of complicated 3-D structures*, in Int. Conf. On Computer-Aided Design, Santa Clara, 1994.
[41] J. Phillips and J. White, *A precorrected-FFT method for electrostatic analysis of complicated 3-D structures*, IEEE Trans. Computer-Aided Design, 16 (1997), pp. 1059–1072.
[42] G. P. M. Poppe and C. M. J. Wijers, *More efficient computation of the complex error function*, ACM Trans. Math. Soft., 16 (1990), pp. 38–46.
[43] C. A. Rozzi, D. Varsano, A. Marini, E. K. U. Gross, and A. Rubio, *Exact Coulomb cutoff technique for supercell calculations*, Phys. Rev. B, 73 (2006), p. 205119.
[44] W. Rudin, *Functional Analysis*, McGraw-Hill, New York, second ed., 1991.
[45] D. S. Shamshirgar and A.-K. Tornberg, *Fast ewald summation for electrostatic potentials with arbitrary periodicity*, arXiv:1712.04732, (2017).
[46] A.-K. Tornberg, *The Ewald sums for singly, doubly and triply periodic elecrostatic systems*, Adv. Comput. Math., 42 (2016), pp. 227–248.
[47] L. Trefethen, *Spectral Methods in Matlab*, Oxford University, 2000.
[48] G. Vainikko, *Fast solvers of the Lippmann-Schwinger equation*, Direct and Inverse Problems of Mathematical Physics, 5 (2000), pp. 423–440.
[49] F. Vico, L. Greengard, and M. Ferrando, *Fast convolution with free-space Green's functions*, J. Comput. Phys., 323 (2016), pp. 191–203.
[50] J. White, J. Phillips, and T. Korsmeyer, *Comparing Precorrected-FFT and fast multipole algorithms for solving three-dimensional potential integral equations*, in Proceedings of the Colorado Conference on Iterative Methods, Breckenridge, Colorado, 1994.
[51] K. Xu and S. Jiang, *A bootstrap method for sum-of-poles approximations*, J. Sci. Comput., 55 (2013), pp. 16–39.
[52] M. R. Zaghloul and A. N. Ali, *Algorithm 916: Computing the Faddeyeva and Voigt functions*, ACM Trans. Math. Soft., 38 (2011), p. 15.